Interference Drag Associated with Engine Locations for Multidisciplinary Design Optimization

Nathaniel J. Blaesser, *
NASA Langley Research Center, Hampton, VA, 23681

Joseph A. Schetz † and Rakesh K. Kapania ‡
Virginia Polytechnic Institute and State University, Blacksburg, VA, 24061

This research aims to quantify the interference drag for various engine locations on a traditional "tube and wing," 150-passenger commercial aircraft flying at 35,000 ft and Mach 0.8. Engine locations are varied in the chordwise, spanwise, and vertical directions near the wing, both under and above the wing, as well as along the fuselage. Euler simulations are performed with representative powered modern engines. The results are intended to supplement empirical drag estimates suitable for multidisciplinary design environments. Large interference drag increases, as compared to the isolated airframe and engine geometry, are found to occur when the engine is placed directly above or below the wing. Interference effects are significantly reduced, and in some instances result in benefits compared to the isolated bodies, when the engines are placed fore or aft of the wing. Interference drag increases are partially explained by flow channels leading to choked flow and shock interactions between bodies.

I. Introduction

Recent research by NASA and industry partners is exploring the effect of engine location on transport aircraft performance parameters such as fuel consumption and noise. This research is driven by propulsion technologies that are enabling ever-increasing bypass ratios, resulting in larger diameter nacelles. Large diameter nacelles create challenges for under-wing engine installations, as larger nacelles frequently require longer landing gear or other design tradeoffs. Additional impetus to explore engine location comes from turboelectric propulsion, which enables the power-producing turbine to be decoupled from the thrust-producing fan. The highly multi-disciplinary nature of this problem means that the design of the aircraft may be driven by not only aero-propulsive performance, but also by noise and structural requirements.

Engine location reflects numerous different requirements and trades. Modern transport aircraft almost exclusively use under-wing mounted engines, though this was not always the case. The Boeing 737 and Douglas DC-9 both entered service near the same time, yet Boeing chose under-wing engines while Douglas chose fuselage-mounted. Sutter lists several reasons why Boeing engineers opted to use under-wing engines on the 737, including ease of on-ground maintenance and concerns about flow distortion from the wing and fuselage entering the inlet if the engines were mounted on the fuselage [1]. Another possible explanation for why fuselage-mounted engines have fallen out of favor for transport aircraft is because the engine attachment removes usable cabin space. Losing cabin space means fewer seats for commercial airlines. Some business jet manufacturers accept this trade-off and use fuselage-mounted engines, likely to keep landing gear short and enable simpler boarding from the tarmac. A notable exception is the HondaJet, which has its engines mounted above the wing to preserve cabin volume [2]. Military aircraft have embedded engines to reduce radar signature and increase survivability, but maintenance costs for embedded engines are too high for non-military applications. Sutter notes that podded engines are much safer than embedded engines, as a failed engine does not risk the structural integrity of the wing [1].

Historically, over-the-wing nacelle (OWN) concepts were considered high drag and were only used for missions requiring the unique benefits of OWN. Depending on the chordwise position of the engine, OWN configurations can provide short takeoff and landing (STOL) capabilities by employing the Coandă effect to keep flow attached to the suction surface of the wing [3]. The upper surface jet also enables removing the thrust gate from the high lift systems on a conventional aircraft. There have been a few examples of transport-sized OWN aircraft, such as the Boeing YC-14

*Aerospace Engineer, Aeronautics Systems Analysis Branch, 1 N. Dryden Street MS 442, Hampton VA, Member
†Holder of Fred D. Durham Chair, Crofton Department of Aerospace and Ocean Engineering, Lifetime Fellow
‡Mitchell Endowed Professor, Crofton Department of Aerospace and Ocean Engineering, Lifetime Associate Fellow

and the Fokker VFW 614. Lockheed Martin's hybrid wing body has also shown promise [4]. In terms of regional or private jets, the HondaJet is the most well-known example of an OWN configuration, though many aircraft in this class feature fuselage-mounted engines that are in essentially the same location along the fuselage. In the realm of distributed propulsion, a number of concept aircraft are being proposed that exploit the ability to place the power-producing turbines separate from the thrust-producing fans. In particular, the NASA N3-X uses wingtip turbines to power a mailbox-slotted fan system. NASA's STARC-ABL uses conventional engines to power under-wing fans and a boundary layer ingesting tailcone thruster.

This paper only focuses on the aerodynamic considerations of engine mounting locations, noting that the selection of an optimal engine location requires consideration and input from additional disciplines. Within this paper, Section II discusses a literature review into the past work on OWN and unconventional engine placements. Section III describes the analysis details and data collection methods. Included are the geometries for the aircraft and engine and the powered boundary conditions for the engine inlet and exhaust planes. Section III also details the approach for controlling lift coefficient and sampling the design space. Section IV presents the results from nearly 200 powered Euler simulations and highlights the observed trends. Section V summarizes the paper and its key conclusions. Section VI describes the future work to be carried out once the data collection is complete.

II. Problem Background

Propulsion-airframe integration (PAI) studies are a challenge during the conceptual design phase because simple aerodynamic models, such as panel and vortex lattice methods, do not correctly account for the interactions and higher-order effects between components. Indeed, Hoerner's comment that, "Strict calculation of interference drag would be complicated and specific methods to solve such problems according to the principles of theoretical aerodynamics, have not really been developed" [5] still remains true today. Canonical textbooks on aircraft design are either silent on the topic [6], provide general regression equations [7, 8], or cite Hoerner's data [9, 10]. Computational fluid dynamics (CFD) remains the best means of modeling PAI, and rapid geometry creation and meshing are enabling technologies for PAI with CFD. Although not specifically related to PAI research, Tétrault, Schetz, and Grossman [11] determined a surrogate model to predict the interference drag between a wing and strut, which has since been used to increase the fidelity of whole aircraft configuration drag prediction [12]. Surrogates are necessary for expansive MDO studies in which hundreds or more configurations are investigated, as analysis tools like CFD are too computationally expensive to use in the optimization loop.

Numerous researchers have investigated OWN concepts using a variety of approaches. Aerodynamic research encompasses full potential solvers [13], Euler CFD [14–16], and full Navier-Stokes CFD [17–19]. These studies have found that OWN configurations can be aerodynamically competitive with, or superior to, under-wing nacelles, given proper placement or via specific wing shaping. These studies typically center around a limited number of configurations, such as the slipper mounted design created by Hahn [17] and the HondaJet configuration [2]. However, Lockheed Martin studied numerous engine locations for a generic tube and wing aircraft [18]. The primary problem of OWN is the flow channels that develop between the nacelle and the wing or fuselage. Berguin [16] was able to ameliorate this by changing the local wing cross section. Without careful pylon design, the interference drag associated with flow channels is made worse as the pylon constrains the flow in the spanwise direction. Hooker, Wick, Zeune, and Agelastos [18] made efforts to model the pylons, and Savoni and Rudnik [20] made pylon design the central focus of their research.

Many of the above studies found that locating the OWN aft of the wing was the aerodynamically optimum location; however, when optimizing for noise, placing the OWN ahead of the wing resulted in the largest reduction in noise [19, 21]. In particular, Berton notes that as bypass ratio increases, the jet noise is reduced and the aft fan noise becomes the dominant engine noise source [21]. Thus, placing the engine ahead of the wing can provide some level of shielding. Structural considerations also impact the choice of OWN position. As a general rule, placing the engines aft of the elastic axis is known to lower the flutter speed, which can be prohibitive for transport aircraft. The HondaJet is able to overcome problems related to flutter because of the relatively small size of the nacelles [22].

NASA is currently investigating the mid-fuselage nacelle (MFN) concept because of its potential for noise reduction [23]. Previous designs of the MFN concept located the engines aft of the wing, though this is not the optimal location for noise shielding [24, 25]. These past studies have focused on the acoustic aspects of MFN, though other considerations such as aerodynamics, stability and control, and structures were also included. In order to make the MFN feasible, the designs feature a double-deck cabin which can accommodate 224 passengers. The double-deck layout enables the nacelles to be mounted to the bulkhead between floors.

III. Configuration, Engine Modeling, and Data Collection

The model under investigation has a static aircraft and engine geometry, with the location of the engine varying relative to the aircraft. The aircraft is expected to operate at 35,000 ft and Mach 0.8 with a standard atmosphere model. Note that the engine is not resized as interference drag varies with engine location. The aircraft geometry is based on the Boeing 737-8 using information from publicly available documents [26, 27] and modeled in OpenVSP [28]. The dynamic location of the engine necessitates a T-tail configuration to ensure that the horizontal stabilizer would not be in the exhaust. For this aircraft, the tail is representative of a Boeing 717 [29]. For simplicity, the model aircraft does not have pylons connecting the airframe to the engine. Generally, the aerodynamic goal of a pylon is to be as unobtrusive as possible; thus, the current analysis neglects pylons and assumes that the result for a given engine location represents the best possible scenario. Figure 1 shows the reference aircraft geometry used to conduct this study, without the engines.

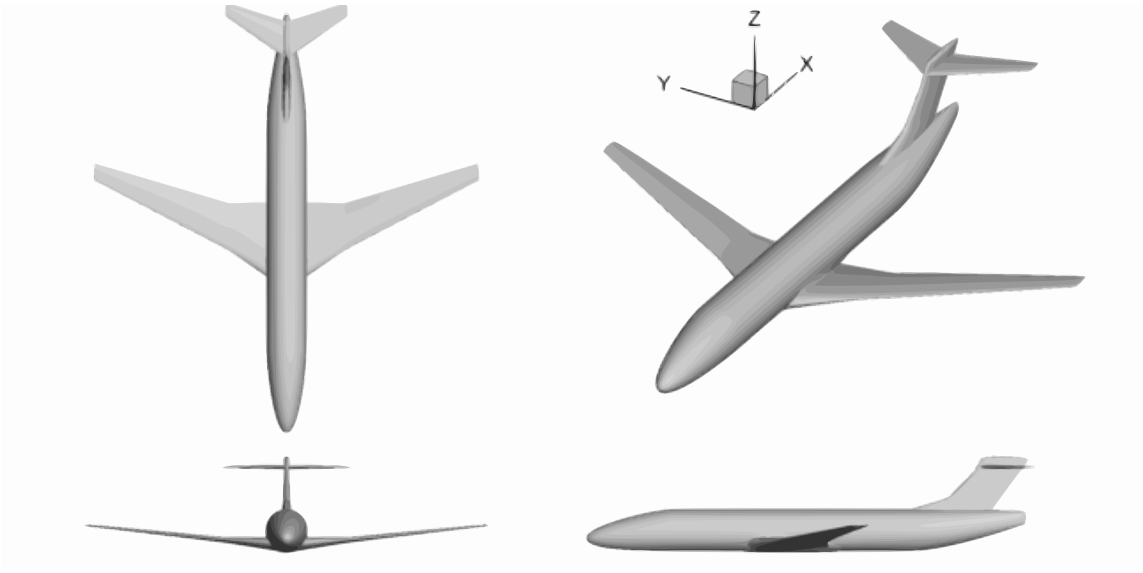

Fig. 1 Three view of the reference aircraft without engines.

The root airfoil for the wing was selected from Selig's airfoil database at the University of Illinois Urbana-Champaign [30]. The outer airfoils consist of BACJ airfoils, scaled to have thicknesses similar to the actual Boeing 737 [31]. The BACJ airfoil is considered a modern airfoil with good transonic capabilities. The wing twist was obtained via Cart3D's shape optimization to minimize drag and achieve the target C_L[32]. The resulting wing has 3.5° of twist, which is in accordance with recommendations for good stall characteristics [33].

The engine model is based on the CFM Leap 1-B, which powers the Boeing 737-8. The model engine has the same bypass ratio, 9:1, and fan diameter, 69 inches, as the Leap 1-B. In order to calculate the engine performance, boundary conditions, and exhaust areas, a simple zeroth-order engine model was used. In a traditional engine model, the power generated by the core would be consumed by the fan, but this requires detailed knowledge of the core's inner workings, which are not publicly available. To overcome this issue, the authors set a net thrust target, which is equal to the gross fan and core thrust, less the ram drag. Knowing the flight conditions, Mach number and altitude, the inlet conditions can be calculated using the isentropic flow relations. The mass flow through the fan and core is easily determined given the bypass ratio. Mattingly commonly employs a fan face Mach number of 0.5, and that value is also adopted here [34]. One can calculate the gross fan thrust by assuming a fan pressure ratio, here taken to be 1.5, and choked flow at the exhaust. To determine the core exhaust conditions, the gross thrust and mass flow are used from the previous steps. If one assumes that the core flow is choked and that the stagnation pressures of the fan and core exits are approximately equal, then the system is closed and one can find the core exhaust conditions[35, 36]. This simplified modeling approach is a good approximation for standard turbofan engines like the one employed in this study. As a further check, the gross thrust of the core should be approximately 25% of the total gross thrust, which holds true here.

Figure 2 shows the engine with the inlet and exhaust planes. To simplify the analysis and avoid the need to model the subsonic diffuser section, the inlet plane is specified at the highlight area. Similarly, the exit planes are located where the fan and core nacelles end, which avoids the need to model the ducting from the fan or turbine to the exhaust.

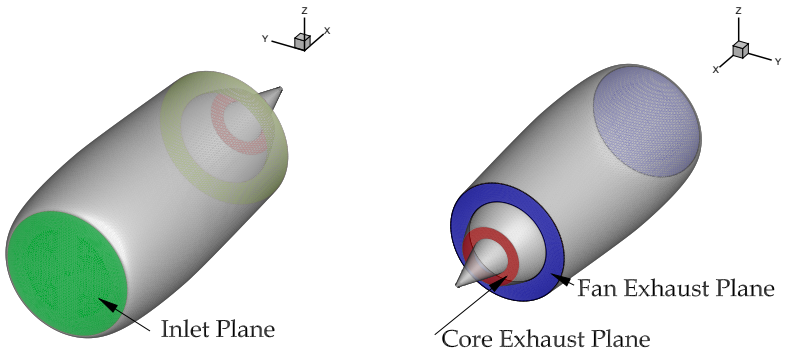

Fig. 2 Inlet and exhaust planes on the engine model.

The baseline aircraft with engines isolated, one semispan length from the body in each direction, was simulated in Cart3D. The isolated engine case determined a baseline inviscid drag by capturing the induced, wave, and pressure drag of the aircraft. To account for viscous drag, *FRICTION* [37] was used. The viscous drag approximation was not updated for each engine location to account for velocity changes due to interference. Together, the coefficient of drag for the isolated airframe and engine was predicted to be 0.034 at a C_L of 0.51 and an angle of attack of zero. This value is reasonable for a modern commercial transport [38].

Figure 3 shows the half-body isolated aircraft with contours of coefficient of pressure, C_p. These contours are important to the results presented in Section IV because the data suggest that placing the engines in areas of high C_p reduces the interference drag.

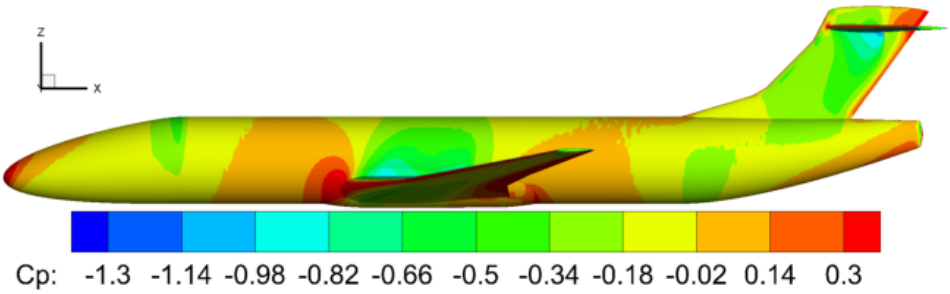

Fig. 3 Contours of C_p on the upper surfaces of the isolated aircraft.

An example mesh and associated Mach number contours are shown in Fig. 4 for a streamwise plane through the centerline of the engine. This particular case has the engine located one engine length ahead of the leading edge, near 30% semispan and one diameter below the wing. The native Cart3D mesh refinement is able to resolve flow features unique to each engine location. Apparent in the figure is the mesh refinement aft of the engine. Here the solver is resolving the exhaust plume as it travels downstream of the wing. Another point of refinement is along the leading edge, with moderate refinement near the upper surface shocks.

The adjoint mesh refinement provides discretization error estimates on the functional, which can allow the user to understand if the phenomenon observed is significant, or within the noise of the data [32]. For this analysis, the functional is the drag on the non-propulsive surfaces (all surfaces except the inlet planes, exhaust planes, and surfaces within the exhaust flow). The near-body flowfield, including shocks and engine exhaust, have undergone significant refinement. A typical mesh consists of approximately seven million cells when fully refined. Each Cart3D solution and mesh refinement can be completed in approximately 75 minutes using 188 cores of Intel Xeon CPU E7-8890 v4. processors.

Figure 5 shows a representative plot of discretization error for a successfully converged case. The error bars in the plot represent the discretization error, which should steadily decrease as the mesh is refined. Successful cases show a convergence within a handful of drag counts, whereas error in an unsuccessful case is considerably higher. Unsuccessfully converged cases are discarded from further analysis.

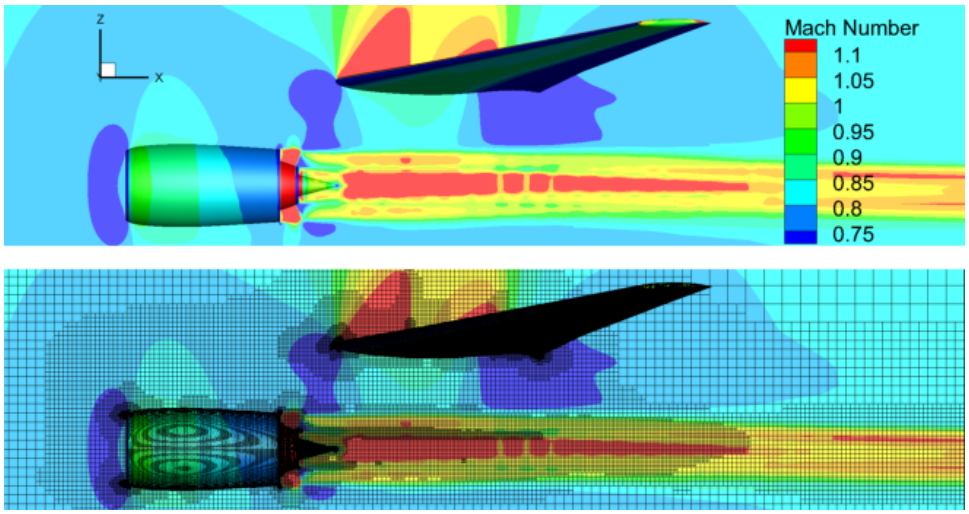

Fig. 4 Sample mesh and Mach number contours for the same view.

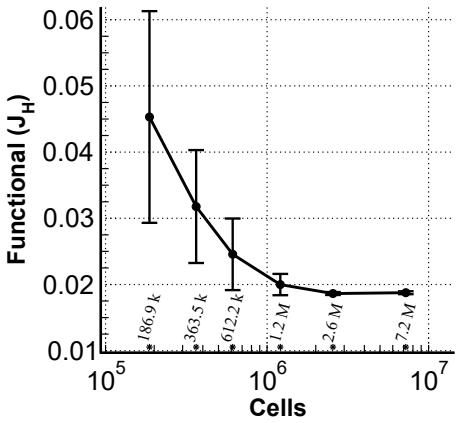

Fig. 5 Discretization error on a successful converged mesh.

The simulations control the angle of attack to ensure that the C_L is near the target C_L. The target C_L is 0.51, which is based on a mid-cruise weight at cruise altitude and Mach number. The engine's location does influence the aircraft's C_L, because the engine will disrupt the clean wing lift distribution. As an example, Fig. 6 shows the lift distribution for two OWN locations where η is the non-dimensional span. The engines are at the same spanwise location and height, but the chordwise location has changed. The midwing engine case has a greater C_L, which means a reduced angle of attack is required to match the target C_L.

A. Engine Location Coordinates

Two coordinate systems were used to specify the engine placement, with the note that the engine location was defined at the center of the engine highlight. These systems rely on the aircraft coordinate system, where x is the streamwise direction, y is the spanwise direction, and z is the vertical direction. The first system, called the fuselage coordinate system, is a cylindrical coordinate system centered on the fuselage. Within this system, ξ_f defines the engine location by the distance from the nose, the distance between the edge of the nacelle and the edge of the fuselage, normalized on the maximum nacelle diameter, Δr, and the angle made between the engine and the horizontal, θ. Figure 7a shows how this is implemented graphically. Using this system, it becomes simple to run sweeps of engine locations where two of the coordinates are held constant.

The second coordinate system, called the wing coordinate system, uses local wing coordinates, defined in Equations 1–3. The non-dimensional chordwise position, ξ_w, is defined such that $\xi_w = 0$ when the aft of the nacelle aligns with

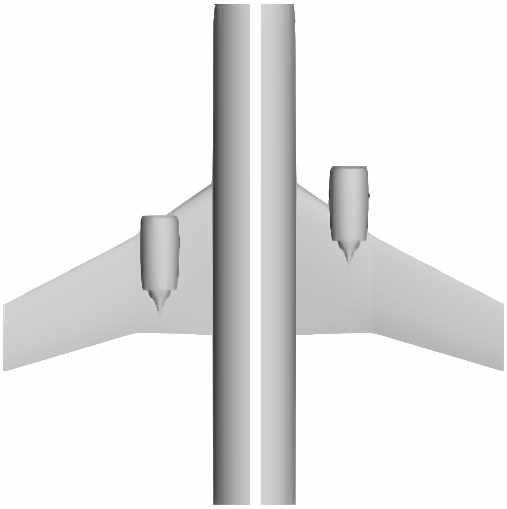

(a) Two typical over wing nacelle locations on the aircraft

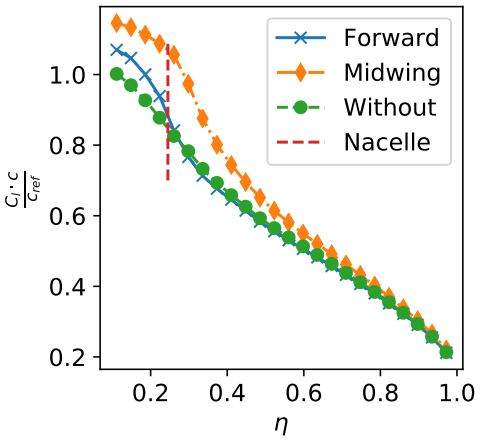

(b) Lift distribution across the wing at zero angle of attack

Fig. 6 Effect of engine location on the lift distribution for the wing.

the leading edge, and $\xi_w = 1$ when the front of the inlet aligns with the trailing edge. These rules hold regardless of the spanwise coordinate, η. The vertical offset, ζ is defined as the distance above the leading edge of the wing, defined in Eq. 3, where z is the vertical location, $z_{LE}(\eta)$ is the vertical coordinate at that specific spanwise station, and D is the nacelle maximum diameter. (Due to wing twist, a constant ζ value will have different absolute heights above the wing as ξ_w varies.) Defining this system is unintuitive because of wing sweep and taper, thus the engine's lengh-to-chord ratio varies with spanwise position, and the leading edge coordinate varies. The advantage of this system is that it is easy to define coordinates that are guaranteed to not overlap with the wing. The results section will show that having overlap between the nacelle and wing typically leads to higher drag numbers. Figure 7a shows a planview of a simple wing, with engines placed at various spanwise locations (varying η). Here the chordwise position is held constant at $\xi_w = 0.25$. Because $0 \leq \xi_w \leq 1$, the engines will overlap the wing, though in a varying amount. Near the tip, where the chord is small, the engine overlaps the wing entirely.

$$\xi_w = \frac{x - x_{LE}(\eta) + L}{c(\eta) + L} \tag{1}$$

$$\eta = \frac{y}{b/2} \tag{2}$$

$$\zeta = \frac{z - z_{LE}(\eta)}{D} \tag{3}$$

IV. Results

A. Data Analysis

In the subsequent sections, plots of change in drag counts, or ΔC_D, are presented. This metric is defined in Eq. 4. A negative value indicates that the given engine location resulted in less drag than the isolated engine/aircraft, whereas a positive number indicates higher drag.

$$\Delta C_D = (C_{D,case} - C_{D,isolated}) \times 10000 \tag{4}$$

Thus, one can determine the amount of interference between the bodies and whether this interference is beneficial or detrimental. The baseline aircraft has roughly 340 drag counts, which is important when assessing the impact of engine location.

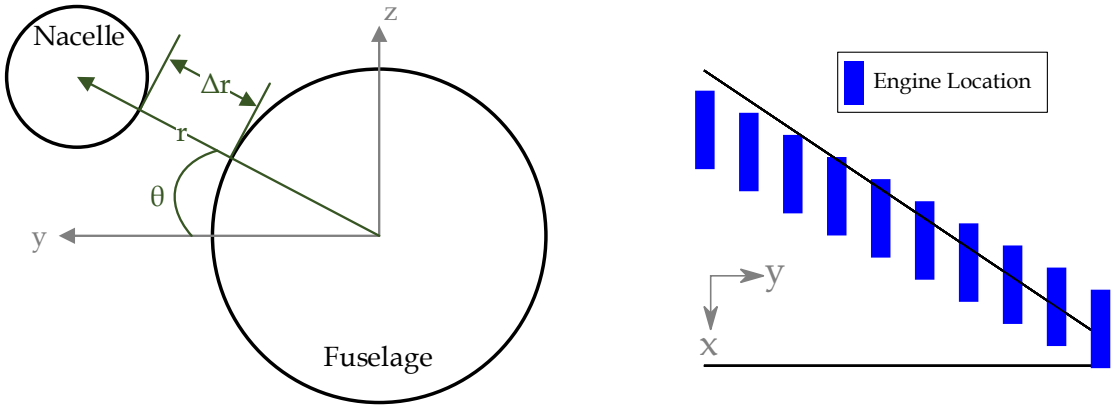

(a) Fuselage coordinate frame, ξ_f runs into the page **(b) Wing coordinate frame. In this figure, $\xi_w = 0.25$**

Fig. 7 Visual description of the coordinate systems used to define engine locations.

Using Cart3D's error estimate, a typical case will converge to within ±2 drag counts. The error estimate provides greater confidence that the trends observed are outside the noise caused by changes in mesh or other effects. Similarly, the C_L falls within 2% of the target value for all cases, ensuring a fair drag comparison. Recall the induced drag, C_{Di}, changes with C_L. A common estimate, using Eq. 5, would imply that a 2% change in C_L can lead to another ±2 counts of drag. Within Eq. 5, e is the span efficiency factor and $\mathcal{AR}$ is the wing's aspect ratio.

$$C_{Di} = \frac{C_L^2}{\pi e \mathcal{AR}} \tag{5}$$

Figure 8 provides an overview of the nearly 200 analysis cases run thus far, with the right side of the aircraft showing the discrete points and the cubes colored to show ΔC_D. These points were selected to observe general trends, not to sample the space in order to support a surrogate model. This ad hoc approach explains why there are large gaps in some regions, and clusters of points in others. Future work will include more samples, using space-filling strategies to create a surrogate model. The cases show engine location sweeps along the fuselage and various wing analysis runs to determine the impact of wing/nacelle interaction.

B. Near-Wing Locations

The contour surface on the left of Fig. 8 is a linear interpolation between points along a constant spanwise location. The interpolation should not be used as a means of prediction, but it clarifies the overarching trends in the data. The first observation is the high drag increase when the engine is placed directly above the wing. Here, the increase in drag can be in excess of 150 drag counts, thus making the location infeasible. The contour plot shows that the largest drag benefit is obtained with the conventional installation (front and below the wing), but also at the location above and immediately aft of the wing. The drag numbers for these locations are on par with one another, implying that the aft location is feasible from an aerodynamic perspective. This location also agrees with past studies, that have shown aft and above the wing to be aerodynamically optimum. Part of the reason this area has potential is because the engine is located downstream of the wing shock, where the flow is slower. This is visible in Fig. 3, where the C_p is relatively high just aft of the wing. One major concern with this flow would be heavy distortion at the fan. This analysis is unable to consider the effect of flow distortion on engine performance, but it must be considered before moving forward with this configuration.

Engines located directly above the wing are infeasible due to the shocks that exist on the upper surface of the wing. Figure 9 shows Mach number contours cut through the center of the engine when the engine is located at approximately 35% of the semispan. The shock terminating near the aft of the nacelle contributes to a large reduction in momentum, and the choked flow drastically alters the engine exhaust path coming out of the engine by forcing it up away from the wing. This type of effect is common when the flow is already supersonic, or is nearly so. For this reason, placing the engine near the suction side of the lifting surfaces like the wing or empennage will likely lead to unacceptable drag increases. Moving the engine directly under the wing shows promise as an alternative, but it is not superior to the current engine location and exacerbates the issue of ground clearance.

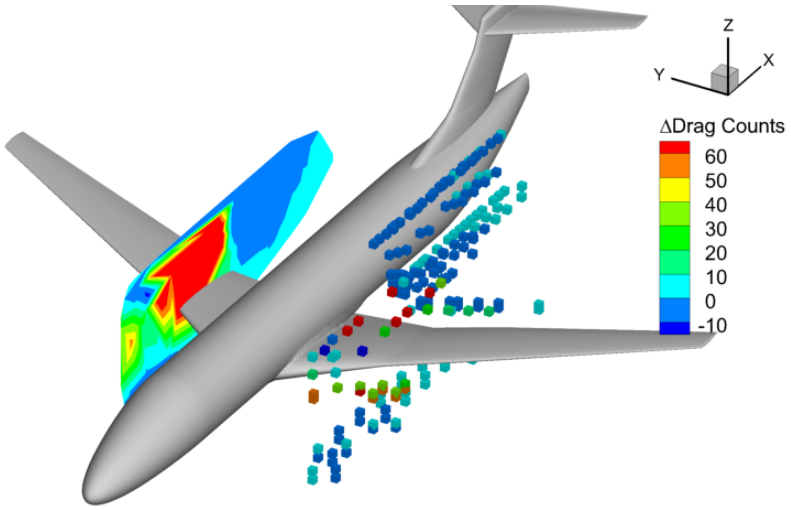

Fig. 8 Summary of all analysis cases. Data points on the right represent the center of the engine highlight. On the left is a contour surface showing the change in drag as a function of engine location.

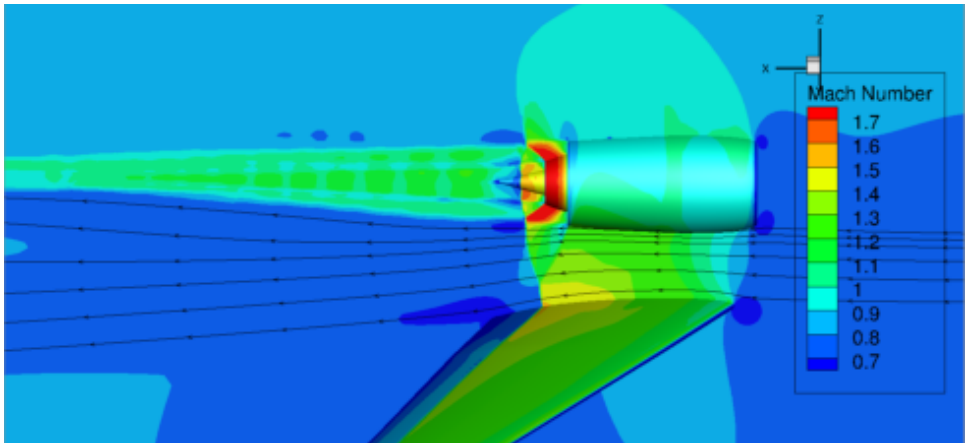

Fig. 9 Flow between the nacelle and wing, when the nacelle is over the wing. A shock is formed that interacts with the exhaust plume, causing a significant increase in drag.

C. Fuselage-Mounted Locations

Multiple sweeps of engine location along the fuselage were conducted to quantify the impact of moving the engine aft. For these sweeps, the y- and z-location does not change (Δr and θ in fuselage coordinates). Figure 10 shows the engine location as viewed from the front of the aircraft and its corresponding drag profile as the engine moves aft. The dominant trend is that as the engine moves further aft, the drag increases. Increasing radial distance has a smaller effect on the drag. Figure 10a shows the diminishing returns gained through increasing the radial distance of the engine. Moving the engine from a Δr of 0.27 to 0.54 decreases the interference drag, but increasing the radial offset to 0.81 shows little benefit. Within Fig. 10b, the interference drag across every Δr value is similar, and as the engine moves aft, the installation drag trends toward zero. This implies that, when mounted high on the fuselage, the drag is relatively insensitive to engine location.

Once again referencing Fig. 3, there is a drop in C_p near the start of the aft taper region on the underside of the aircraft. This corresponds to engine locations with low mount angles, like that of Fig. 10a, and explains the increase in drag as the engine is moved aft. When the engine is mounted high, such as Fig. 10b the engine is not exposed to this accelerated airflow; thus, the flow is not choked.

Figure 11 shows surface contours of Mach on the engine and fuselage for two separate engine locations. In both images, the engine is in the upper-fuselage position shown in Fig. 10b. The upper image has the engine further aft,

where the interference from the vertical tail is clearly visible. In the lower image, the flow is not choked between the nacelle and fuselage; thus, no shock is formed.

This analysis, for the sake of simplicity, kept the tail size and wing location constant for all engine locations. In reality, the tail size would change based on pitching moment and other requirements, and the wing would move substantially with aft-mounted nacelles. This creates some potential opportunities that can be explored further. Most aircraft with fuselage-mounted engines, such as the Boeing 717, have the wing mounted much further aft than aircraft with engines mounted to the wing. Moving the wing back enables shorter landing gear for the same tail strike angle, which has its own benefits in terms of weight and noise. Additionally, with a further aft wing, the carry-through for the nacelles may be far enough back such that it does not occupy significant cabin space. These trades are outside the scope of the current paper and are left as future work.

V. Concluding Remarks

This paper focused on quantifying the interference drag of a high bypass ratio turbofan on a single-aisle transport aircraft. The drag values for a variety of engine locations were calculated using inviscid CFD, and the viscous drag was estimated using a drag build-up approach. The motivation for investigating new engine locations stems from the need to accommodate ever-increasing bypass ratios as well as the expanded design space enabled by electric propulsion.

This presented work established a process for rapidly determining the interference drag of a high bypass ratio engine on a given airframe. This analysis showed that much of the drag could be predicted simply by looking at the isolated contours of pressure coefficient to determine where the flow would choke with the addition of a nacelle. To illustrate this, several CFD runs were performed with the engine in close proximity to lifting surfaces like the wing and vertical tail. When the engine was placed above the wing, the interaction of the existing upper surface shock with the nacelle increased the drag on the order of 150 counts. These results show that, when strategically located, over-the-wing nacelles or fuselage-mounted nacelles can have beneficial drag characteristics. When considering fuselage-mounted locations, the key criterion is to prevent shocks between the nacelle and fuselage or vertical tail. This can be accomplished by increasing the offset distance between the engine and fuselage, but there are rapidly diminishing returns to this approach.

VI. Future Work

The analysis performed thus far has focused on determining the best engine location from an aerodynamic perspective. Future work will focus on understanding the data to enable an interference drag prediction based on surrogate models for inclusion in multidisciplinary design optimization studies. This is important because engine location cannot be dictated solely by aerodynamics. The position aft and above the wing may be well-suited aerodynamically, but wing mounting can lead to reduced flutter speed, and fuselage mounting may reduce seating capacity.

Acknowledgments

This study was supported by NASA's Advanced Air Transport Technology Project in the Systems Analysis and Integration element.

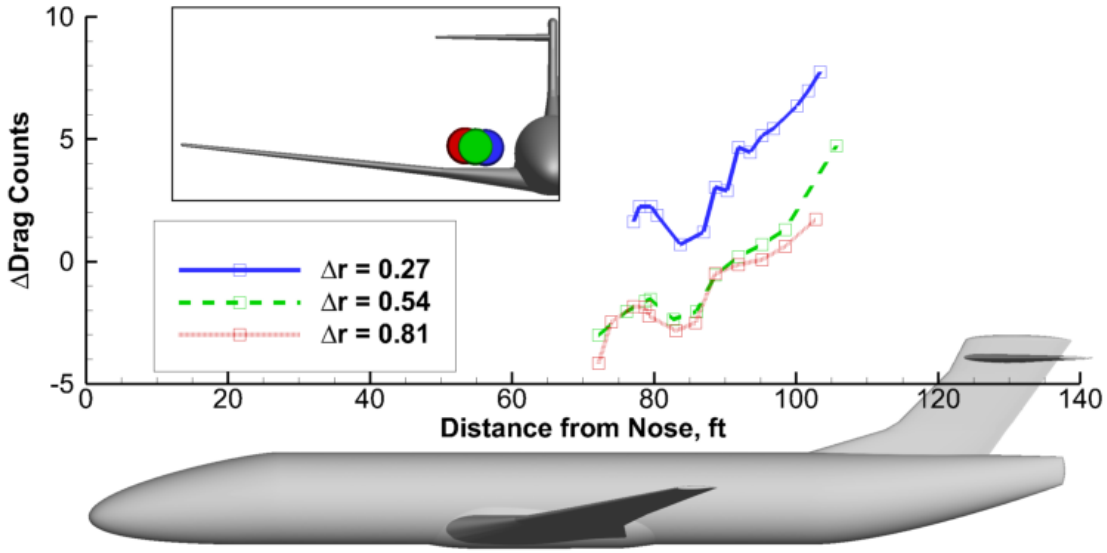

(a) Engine mounted just above the wing, θ = 5.0°.

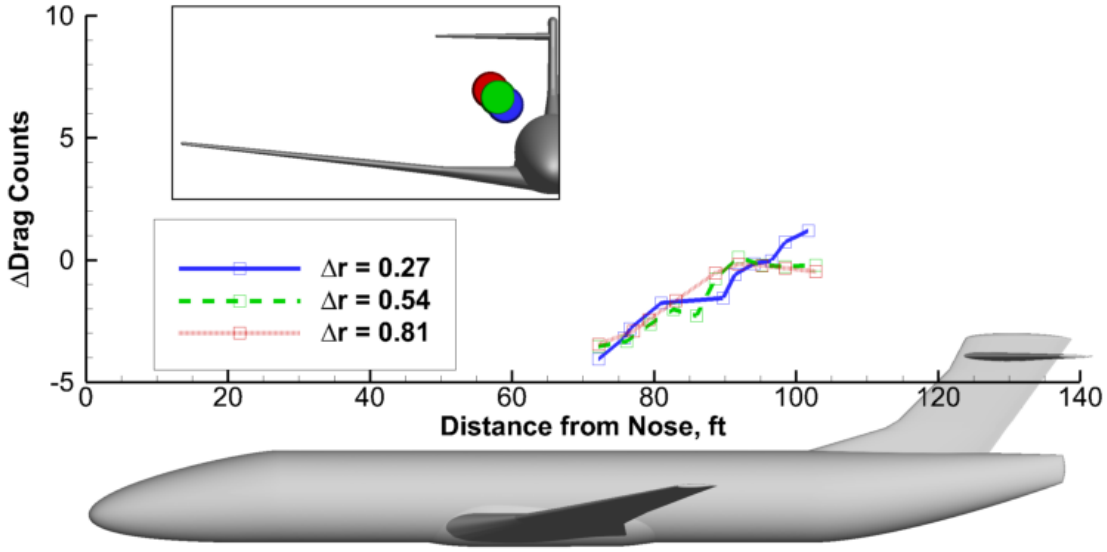

(b) Engine mounted high on the fuselage, θ = 45°.

Fig. 10 Sweeps of ξ_f-location for various θ and Δr values in the fuselage coordinate system to determine change in C_D from the isolated aircraft-engine case.

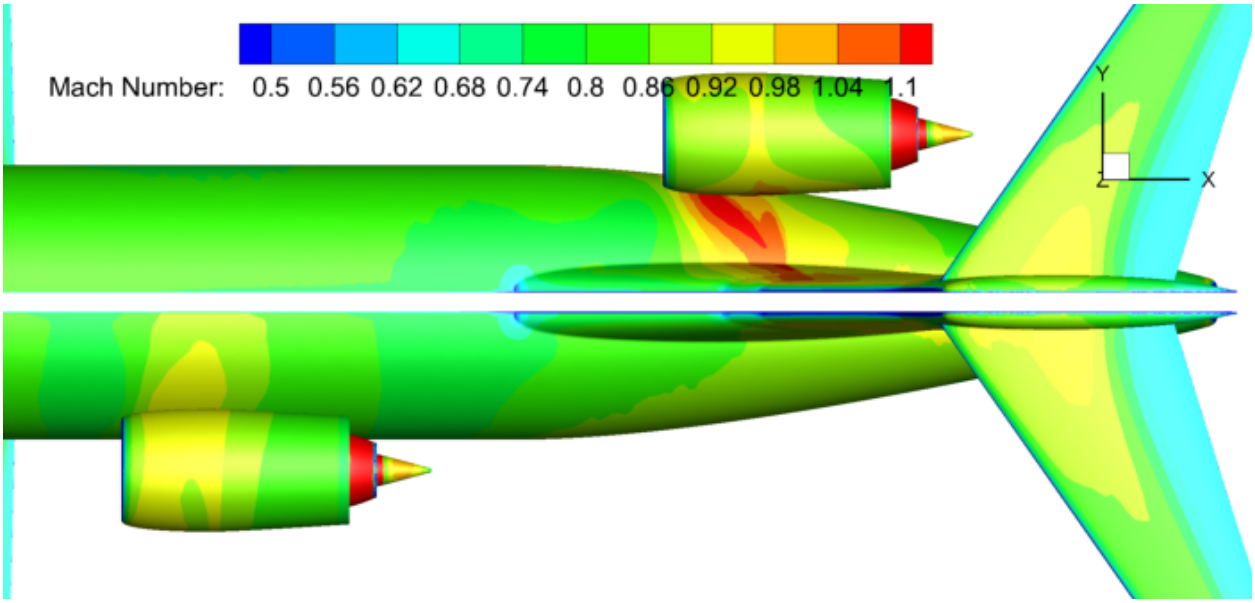

Fig. 11 Contours of Mach on the aircraft surface for two engine locations. As the engine moves aft, the flow is choked between the nacelle and vertical tail, leading to higher drag.

References

[1] Sutter, J., and Spenser, J., *747: Creating the World's First Jumbo Jet and Other Adventures from a Life in Aviation*, Smithsonian Books, 2006.

[2] Fujino, M., "Design and Development of the HondaJet," *Journal of Aircraft*, Vol. 42, No. 3, 2005, pp. 755–764.

[3] Nelson, B., *STOL Progenitors: The Technology Path to a Large STOL Aircraft and the C-17A*, AIAA, 2002.

[4] Wick, A. T., Hooker, J. R., Walker, J., Chan, D. T., Plumley, R., and Zeune, C., "Hybrid Wing Body Performance Validation at the National Transonic Facility," AIAA SciTech Forum, American Institute of Aeronautics and Astronautics, 2018. doi:10.2514/6.2017-0099, URL https://doi.org/10.2514/6.2017-0099.

[5] Hoerner, S. F., *Fluid-Dynamic Drag*, Sighard Hoerner, 1965.

[6] Nicolai, L. M., and Carichner, G. E., *Fundamentals of Aircraft and Airship Design*, AIAA Education Series, 2010.

[7] Raymer, D. P., *Aircraft Design: A Conceptual Approach*, AIAA Education Series, 2012.

[8] McCormick, B., *Aerodynamics, Aeronautics and Flight Mechanics*, Wiley, 1995.

[9] Roskam, J., and Lan, C.-T. E., *Airplane Aerodynamics and Performance*, DARcorporation, 1997.

[10] Torenbeek, E., *Advanced Aircraft Design*, John Wiley & Sons, 2013.

[11] Tetrault, P.-A., Schetz, J., and Grossman, B., "Numerical prediction of the interference drag of a streamlined strut intersecting a surface in transonic flow," Aerospace Sciences Meetings, American Institute of Aeronautics and Astronautics, 2000. doi:10.2514/6.2000-509, URL https://doi.org/10.2514/6.2000-509.

[12] Gur, O., Mason, W., and Schetz, J., "Full Configuration Drag Estimation," Fluid Dynamics and Co-located Conferences, American Institute of Aeronautics and Astronautics, 2009. doi:10.2514/6.2009-4109, URL https://doi.org/10.2514/6.2009-4109.

[13] Kinney, D., Hahn, A., and Gelhausen, P., "Comparison of low and high nacelle subsonic transport configurations," Fluid Dynamics and Co-located Conferences, American Institute of Aeronautics and Astronautics, 1997. doi:10.2514/6.1997-2318, URL https://doi.org/10.2514/6.1997-2318.

[14] Fujino, M., and Kawamura, Y., "Wave-Drag Characteristics of an Over-the-Wing Nacelle Business-Jet Configuration," *Journal of Aircraft*, Vol. 40, No. 6, 2003, pp. 1177–1184. doi:10.2514/2.7207, URL https://doi.org/10.2514/2.7207.

[15] Sasaki, D., and Nakahashi, K., "Aerodynamic Optimization of an Over-the-wing-nacelle-mount Configuration," *Model. Simul. Eng.*, Vol. 2011, 2011. doi:10.1155/2011/293078, URL http://dx.doi.org/10.1155/2011/293078.

[16] Berguin, S., and Mavris, D., "Interactions in Over-Wing Nacelle Optimization," Aerospace Sciences Meetings, American Institute of Aeronautics and Astronautics, 2013. doi:10.2514/6.2013-25, URL https://doi.org/10.2514/6.2013-25.

[17] Hill, G. A., Kandil, O. A., and Hahn, A. S., "Aerodynamic Investigations of an Advanced Over-the-Wing Nacelle Transport Aircraft Configuration," *Journal of Aircraft*, Vol. 46, No. 1, 2009, pp. 25–35. doi:10.2514/1.39730, URL https://doi.org/10.2514/1.39730.

[18] Hooker, J. R., Wick, A., Zeune, C. H., and Agelastos, A., "Over Wing Nacelle Installations for Improved Energy Efficiency," Fluid Dynamics and Co-located Conferences, American Institute of Aeronautics and Astronautics, 2013. doi:10.2514/6.2013-2920, URL https://doi.org/10.2514/6.2013-2920.

[19] Powell, S., Sóbester, A., and Joseph, P., "Performance and Noise Trade-Offs on a Civil Airliner with Over-the-Wing Engines," Aerospace Sciences Meetings, American Institute of Aeronautics and Astronautics, 2011. doi:10.2514/6.2011-266, URL https://doi.org/10.2514/6.2011-266.

[20] Savoni, L., and Rudnik, R., "Pylon Design for a Short Range Transport Aircraft with Over-the-Wing Mounted UHBR Engines," AIAA SciTech Forum, American Institute of Aeronautics and Astronautics, 2018. doi:10.2514/6.2018-0011, URL https://doi.org/10.2514/6.2018-0011.

[21] Berton, J. J., "Noise Reduction Potential of Large Over-the-Wing Mounted, Advanced Turbofan Engines," NASA-TM-2000-210025, NASA, Cleveland, OH, April 2000.

[22] Fujino, M., Oyama, H., and Omotani, H., "Flutter Characteristics of an Over-the-Wing Engine Mount Business-Jet Configuration," Structures, Structural Dynamics, and Materials and Co-located Conferences, American Institute of Aeronautics and Astronautics, 2003. doi:10.2514/6.2003-1942, URL https://doi.org/10.2514/6.2003-1942.

[23] Guo, Y., Thomas, R. H., Clark, I., and June, J., "Far Term Noise Reduction Roadmap for the Mid-Fuselage Nacelle Subsonic Transport," AIAA AVIATION Forum, American Institute of Aeronautics and Astronautics, 2018. doi:10.2514/6.2018-3126, URL https://doi.org/10.2514/6.2018-3126.

[24] Guo, Y., Nickol, C. L., Burley, C. L., and Thomas, R. H., "Noise and Fuel Burn Reduction Potential of an Innovative Subsonic Transport Configuration," AIAA SciTech Forum, American Institute of Aeronautics and Astronautics, 2014. doi:10.2514/6.2014-0257, URL https://doi.org/10.2514/6.2014-0257.

[25] Bonet, J. T., Schellenger, H. G., Rawdon, B. K., Elmer, K. R., Wakayama, S. R., Brown, D. L., and Guo, Y., "Environmentally Responsible Aviation (ERA) Project - N+2 Advanced Vehicle Concepts Study and Conceptual Design of Subscale Test Vehicle (STV)," Contractor Report CR-2011-216519, NASA, 2011.

[26] Jackson, P. (ed.), *IHS Jane's All the World's Aircraft*, IHS, 2016-2017.

[27] *737 Max Airplane Characteristics for Airport Planning*, The Boeing Company, Aug. 2017. doi:D6-38A004, d6-38A004 Rev A.

[28] Hahn, A., "Application of Cart3D to Complex Propulsion-Airframe Integration with Vehicle Sketch Pad," Aerospace Sciences Meetings, American Institute of Aeronautics and Astronautics, 2012. doi:10.2514/6.2012-547, URL https://doi.org/10.2514/6.2012-547.

[29] *717-200 Airplane Characteristics for Airport Planning*, The Boeing Company, Nov. 2014. doi:D6-58330B, d6-58330B.

[30] Selig, M., "Boeing 737 Root Airfoil (b737a-il)," , Nov. 2018. URL http://airfoiltools.com/airfoil/details?airfoil=b737a-il, accessed Nov. 15, 2018.

[31] Segee, M., Schetz, J. A., and Kapania, R. K., "Transonic Aerodynamics Analysis for Multidisciplinary Design Optimization Applications," AIAA AVIATION Forum, American Institute of Aeronautics and Astronautics, 2016. doi:10.2514/6.2016-4039, URL https://doi.org/10.2514/6.2016-4039.

[32] Nemec, M., and Aftosmis, M., "Output Error Estimates and Mesh Refinement in Aerodynamic Shape Optimization," No. 0 in Aerospace Sciences Meetings, American Institute of Aeronautics and Astronautics, 2018. doi:10.2514/6.2013-865, URL https://doi.org/10.2514/6.2013-865.

[33] Cummings, R. M., Mason, W. H., Morton, S. A., and McDaniel, D. R., *Applied Computational Aerodynamics: A Modern Engineering Approach*, Cambridge Aerospace Series, 2015.

[34] Mattingly, J. D., Heiser, W. H., and Pratt, D. T., *Aircraft Engine Design*, second edition ed., AIAA Education Series, Reston, VA, 2002.

[35] Guha, A., "Optimum Fan Pressure Ratio for Bypass Engines with Separate or Mixed Exhaust Streams," *Journal of Propulsion and Power*, Vol. 17, No. 5, 2001, pp. 1117–1122. doi:10.2514/2.5852, URL https://arc.aiaa.org/doi/abs/10.2514/2.5852.

[36] Mattingly, J. D., *Elements of Propulsion*, AIAA Education Series, AIAA, 1801 Alexander Bell Drive, Reston, VA 20191, 2006.

[37] Mason, W. H., *FRICTION - from the Virginia Tech Aerodynamics and Design Software Collection*, Virginia Polytechnic Institute and State University, Blacksburg, VA, Feb. 2015. URL http://www.dept.aoe.vt.edu/~mason/Mason_f/MRsoft.html#SkinFriction.

[38] Bradley, M. K., and Droney, C. K., "Subsonic Ultra Green Aircraft Research: Phase II-Volume II-Hybrid Electric Design Exploration," Tech. rep., NASA/CR-2015-218704, NASA Langley Research Center, Hampton, VA, 2015.